JVST A
Journal of Vacuum Science & Technology A

ARTICLE

pubs.aip.org/avs/jva

Promoting subsurface Sn incorporation at Nb(100) oxide surface sites leading to homogeneous Nb_3Sn film growth for superconducting radiofrequency applications

Cite as: J. Vac. Sci. Technol. A **42**, 063204 (2024); doi: 10.1116/6.0003892
Submitted: 10 July 2024 · Accepted: 9 September 2024 ·
Published Online: 30 September 2024

Sarah A. Willson,[a] Rachael G. Farber,[b] and S. J. Sibener[c]

AFFILIATIONS

Department of Chemistry, The James Franck Institute, The University of Chicago, 929 E. 57th Street, Chicago, Illinois 60637

Note: This paper is part of the Special Topic Collection Honoring John Ekerdt's Contributions to Chemical Reaction Engineering and Surface Chemistry for Electronic Materials.

[a]**Present address:** KLA, 1 Technology Drive, Milpitas, CA 95035
[b]**Present address:** Department of Chemistry, The University of Kansas, 1567 Irving Hill Rd, Lawrence, KS 66045
[c]**Author to whom correspondence should be addressed:** s-sibener@uchicago.edu

ABSTRACT

For next-generation superconducting radiofrequency (SRF) cavities, the interior walls of existing Nb SRF cavities are coated with a thin Nb_3Sn film to improve the superconducting properties for more efficient, powerful accelerators. The superconducting properties of these Nb_3Sn coatings are limited due to inhomogeneous growth resulting from poor nucleation during the Sn vapor diffusion procedure. To develop a predictive growth model for Nb_3Sn grown via Sn vapor diffusion, we aim to understand the interplay between the underlying Nb oxide morphology, Sn coverage, and Nb substrate heating conditions on Sn wettability, intermediate surface phases, and eventual Nb_3Sn nucleation. In this work, Nb-Sn intermetallic species are grown on a single crystal Nb(100) in an ultrahigh vacuum chamber equipped with *in situ* surface characterization techniques including scanning tunneling microscopy, Auger electron spectroscopy, and x-ray photoelectron spectroscopy. Sn adsorbate behavior on oxidized Nb was examined by depositing Sn with submonolayer precision on a Nb substrate held at varying deposition temperatures (T_{dep}). Experimental data of annealed intermetallic adlayers provide evidence of how Nb substrate oxidization and T_{dep} impact Nb-Sn intermetallic coordination. The presented experimental data contextualize how vapor and substrate conditions, such as the Sn flux and Nb surface oxidation, drive homogeneous Nb_3Sn film growth during the Sn vapor diffusion procedure on Nb SRF cavity surfaces. This work, as well as concurrent growth studies of Nb_3Sn formation that focus on the initial Sn nucleation events on Nb surfaces, will contribute to the future experimental realization of optimal, homogeneous Nb_3Sn SRF films.

I. INTRODUCTION

Widespread efforts are underway to coat existing Nb superconducting radiofrequency (SRF) cavities with Nb_3Sn ($T_C \sim 18$ K) thin films to achieve increased accelerating gradients with operating temperatures above that of liquid helium.[1] However, the achievable accelerating gradients of the Nb_3Sn coated cavities are limited by defects and inhomogeneities in the Nb_3Sn film, particularly within the first 100 nm of the surface where superconductivity quenching events are most prevalent.[2] Nb_3Sn has a small superconducting coherence length of ~4 nm, meaning that the superconducting properties of Nb_3Sn films are particularly sensitive to material defects such as stoichiometric inhomogeneities, regions of poor growth, and a high surface roughness.[3–6] Material defects such as Sn rich or poor regions have significantly lower T_C than Nb_3Sn. This can result in localized heating of the Nb_3Sn SRF cavity, leading to quenching of superconducting behavior and a significant decrease in the cavity quality factor. Optimizing the growth of these Nb_3Sn films on polycrystalline Nb SRF cavity surfaces requires a thorough understanding

of how the Nb substrate facilitates the nucleation and incorporation of Sn vapor during alloy growth.

Nb_3Sn films are vulnerable to containing widespread regions with poor growth. These regions can significantly degrade the superconducting properties of coated cavities, especially if the film thickness approaches the superconducting penetration depth of Nb_3Sn (~100 nm).[7] Poor Nb_3Sn film growth on Nb SRF cavities result in RF fields penetrating either to or past the Nb_3Sn /Nb intermetallic interface during SRF operation, where the superconducting properties are reduced as compared to the bulk of the Nb_3Sn film. The persistence of abnormally thin regions of these Nb_3Sn films are a consequence of inhomogeneous Sn coverage during the initial nucleation step.[8] Previous work associated preanodization of the Nb cavity with substantial improvement to Sn nucleation.[9,10] These findings motivate further investigation toward the relationship of the Nb oxidation treatments preceding Sn exposure with the resulting film quality.

Preanodization of the Nb surface often forms a Nb_2O_5 surface layer approximately 70 nm thick,[11] substantially thicker than the ~5 nm native Nb_2O_5 surface oxide. However, during the Nb_3Sn growth recipe for Nb SRF cavities, the cavity undergoes a baking process after it is placed inside the growth furnace. Therefore, the anodized Nb surface is subject to the oxide dissolution mechanisms that are prevalent at the baking temperatures. Typically, the baking, or degas, process results in the Nb cavity remaining between 100 and 200 °C for 24–48 h.[11] After the degas step, the nucleation process commences with Sn vapor (and typically a secondary $SnCl_2$ source) introduced to the Nb cavity held at ~525 °C. A summary of the typical Nb substrate temperatures during each step of the Sn vapor diffusion procedure is shown in Table I.

At the Nb temperatures required for the degas and nucleation steps during the Nb_3Sn growth procedure on SRF cavities, both the anodized (~70 nm) and native (~5 nm) Nb_2O_5 surfaces undergo a reduction process via dissolution of oxygen into the Nb subsurface.[12] Previous work by Oechsner *et al.*[13] and King *et al.*[14] have experimentally studied oxide dissolution kinetics of anodized Nb surfaces. The reduction of Nb_2O_5 to NbO at the Nb surface is driven by the dissolution of the mobile oxygen and follows a first-order reversible reduction reaction between 350 and 450 °C with an activation energy of 174 kJ/mol.[14] The dissolution rate was found to be limited by the oxygen mobility at the oxide-metal interface and is, therefore, independent of the Nb_2O_5 layer thickness.[14]

One important aspect to the Nb surface oxidation is that the formation of Nb_2O_5 produces deep serrations at the metallic Nb interface, significantly increasing the roughness and surface area.[15] The strain introduced by the nucleation of Nb_2O_5 crystallites carve out cracks into the Nb subsurface.[16] During Nb_2O_5 dissolution, the kinetically limited mobility of oxygen atoms drive the reduction process, with the Nb atoms being effectively immobile at 360 °C.[13] The position of the oxide-metallic interface is assumed to remain constant at these moderate dissolution temperatures, with very limited contraction of the Nb atoms in the reducing oxide layer.[13,17] Therefore, the anodized or native Nb_2O_5 surfaces have been reduced to NbO with varying Nb volume densities during the Sn nucleation step (T_{Nb}: 500 °C) of the furnace Nb_3Sn growth procedure. Below the temperatures required for NbO to form ordered reconstructions, the Nb atomic density, NbO surface area, and Sn binding sites are dynamic and determined by the initial Nb_2O_5 layer thickness and the Nb degas procedure.

TABLE I. T_{dep} during the Sn diffusion procedure to form Nb_3Sn coatings on SRF surfaces.

Film growth step	Typical Nb T_{dep}
Nb degas	100–200 °C
Sn nucleation	525 °C
Nb_3Sn coating	1100 °C

In previously published work, we determined that nanoscale sites on the (3 × 1)-O/Nb(100) surface, a highly ordered NbO reconstruction that forms following annealing a Nb(100) crystal > 600 °C, serve as favorable binding sites for Sn adatoms.[18,19] For sub-ML and ML coverages of Sn deposited at 25 °C on pristine and defect-induced (3 × 1)-O/Nb(100) surfaces, we determined that sputter-induced substrate defect sites stabilized the Sn adlayers during postdeposition annealing at T_{anneal} = 500, 700, 800, and 900 °C. Annealing to at least 800 °C was necessary to observe any subsurface Sn incorporation, where Sn is topographically lower than the (3 × 1)-O/Nb(100) terrace, which only occurred at Sn coverages exceeding 1 ML. Between 800 and 900 °C, desorption of the Sn adatoms eventually dominated any subsurface incorporation. Even though these experiments involved sub-ML and ML coverages of Sn deposited at room temperature, it is apparent that the (3 × 1)-O/Nb(100) surface itself does not facilitate the growth of an Nb-Sn intermetallic surface layer. The only favorable Sn binding sites on the (3 × 1)-O/Nb(100) surface corresponded to the "edge" vacancy sites [Fig. 1(a)] that facilitated the lateral diffusion of Sn to form clusters and adlayers [Fig. 1(b)].

While our previous work of Sn adsorption on (3 × 1)-O/Nb(100) demonstrates how the NbO surface structure impacts the behavior of deposited Sn, it is also necessary to elucidate the initial Nb-Sn interactions that occur at the substrate temperatures relevant during realistic Nb_3Sn coating procedures. As described in the preceding paragraphs, the initial Nb oxidation state impacts Sn adsorption and nucleation. Furthermore, the thermal conditions during deposition and adatom concentration both affect the behavior of adsorbed metal layers on oxidized surfaces.[20,21] We also must consider how the higher Sn coverages deposited on Nb surfaces held at an elevated T_{dep} impact the thermal stability of Sn adlayers.

In this work, we explored how substrate preparation processes impact the different Nb surface morphologies that Sn interfaces with during deposition. Scanning tunneling microscopy (STM), x-ray photoelectron spectroscopy (XPS), and Auger electron spectroscopy (AES) data detail how the Nb(100) defect density is dependent on the initial oxidation and maximum annealing temperature reached before and during Sn exposure. Our experiments probe the thermal stability of deposited Sn adlayers to show that temperature-dependent nanoscale NbO defects suppress Sn desorption at deposition temperatures.[19] When depositing Sn on a Nb substrate held at an elevated temperature, the annealing conditions determine the morphology of the thermally reduced NbO surface, ultimately dictating the Sn nucleation pathways. STM data of deposited sub-ML and ML Sn at varying Nb temperatures suggest a

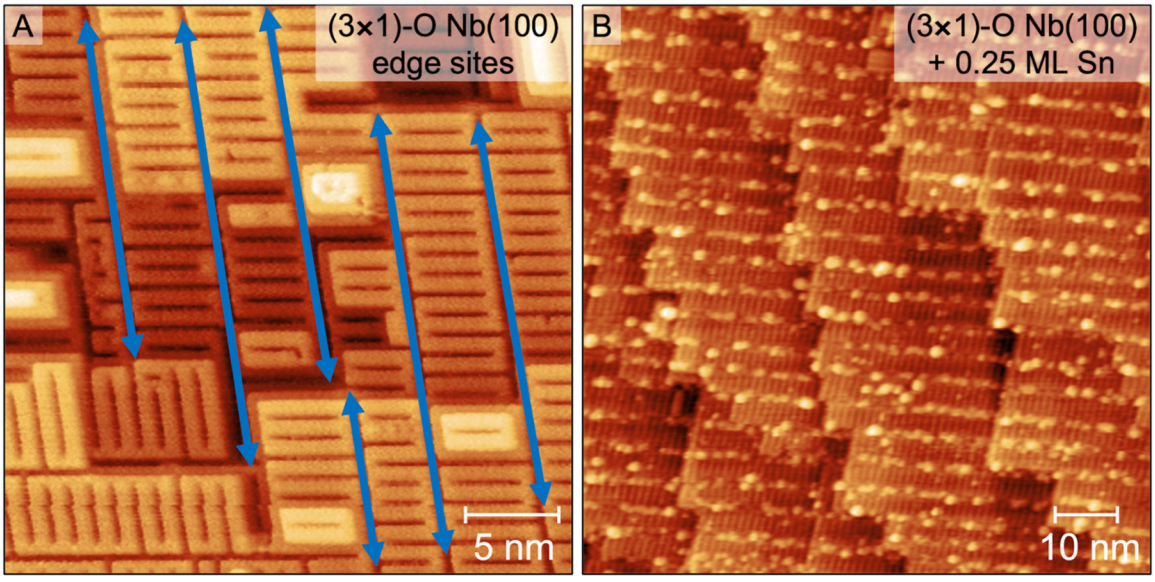

FIG. 1. STM images of the (3 × 1)-O/Nb(100) surface with "edge" sites that serve as preferential sites for Sn island nucleation. The bare (3 × 1)-O/Nb(100) surface in (a) is annotated with blue arrows to denote the "edge" or "vacancies" between the characteristic (3 × 1)-O ladder structure. In (b), the (3 × 1)-O/Nb(100) surface was exposed to 0.25 ML of Sn at T_{dep} 25 °C resulting in Sn island clusters to nucleate along these "edge" sites. (a) −280 mV, 108 pA, 30 × 30 nm^2 and (b) 0.25 ML Sn at T_{dep} 25 °C, 316 mV, 63.2 pA, 90 × 90 nm^2.

threshold for suppressing Sn desorption between $T_{dep} = 780$ and 820 °C. Finally, we examined how increasing the Sn coverage (20 ML) impacts the observed Sn-Nb surface interactions at elevated temperatures. Sn was deposited on Nb(100) surfaces prepared with a near-elemental, NbO, and Nb_2O_5 surface before Sn exposure. XPS and AES data of the Sn/Nb(100) surfaces following deposition and subsequent annealing compare the impact of Nb surface defect sites on the resulting Sn thermal stability. These results demonstrate how parameters such as the Nb(100) surface structure and deposition temperature determine Sn stability at conditions relevant to the Nb_3Sn formation process.

II. EXPERIMENT

All experiments were conducted on a Nb(100) single crystal ($R_a < 0.03\,\mu$m, 99.99% purity, Surface Preparation Laboratory) in the UHV chamber described elsewhere.[12] The pristine NbO reconstruction, (3 × 1)-O/Nb(100), was formed by repeated cycles of Ar^+ ion sputtering (2 kV) and electron beam annealing to 1630 °C. The Nb temperature during annealing and deposition were monitored with an infrared pyrometer (Mikron Infrared, MG-140). *In situ* XPS, AES, and STM confirmed surface cleanliness. The signal intensity produced during AES and XPS analysis were collected by a cylindrical mirror analyzer (CMA, Staib, DESA 100) that was oriented perpendicular to the sample plane. For XPS, we used a Mg anode x-ray source (Specs, XR50) with a 0.34 eV half width at half maximum. There was no monochromator used with the x-ray photon source. The x-ray source was positioned 45° with respect to the sample plane. For AES, a 3.00 keV electron source that is integrated into the CMA was used. The XPS spectra were fitted to Voigt-type functions using the XPST 1.3 Fit Assistant in IgorPro.

To form a clean Nb_2O_5/Nb(100) surface, the (3 × 1)-O/Nb(100) was exposed to atmosphere in the load lock chamber for 5 min. The load lock chamber was vented with evaporated liquid nitrogen and the door of the chamber was cracked open to accommodate atmosphere into the chamber. To form a near-elemental Nb(100) surface, a clean (3 × 1)-O/Nb(100) surface was sputtered with Ar^+ ions (1.5 kV, I_{ion}: 3.5 μA) for 5 min.

For the higher coverage Sn deposition experiments in Sec. III C, the Nb(100) surfaces were exposed to 20 ML equivalence of Sn vapor (99.998%, Kurt Lesker) evaporated at a constant flux for 20 min from an electron beam evaporator source (EFM3 T, Focus GmbH). During elevated temperature depositions, the Nb(100) crystal was heated via electron beam annealing. The selected deposition temperature was reached before Sn exposure and was held constant throughout the deposition procedure. Postdeposition annealing of the multilayer Sn depositions was done for 20 min at 800, 900, and 1000 °C. Clean, deposited, and annealed Nb(100) surfaces were characterized with *in situ* STM, AES, XPS analysis.

III. RESULTS AND DISCUSSION

A. AES and XPS characterization of annealed Nb_2O_5/Nb(100)

Box plot distributions of the O/Nb ratios from AES for the (3 × 1)-O/Nb(100) and native Nb_2O_5/Nb(100) surfaces are plotted in Figs. 2(a) and 2(b), respectively. The (3 × 1)-O/Nb(100) ladder

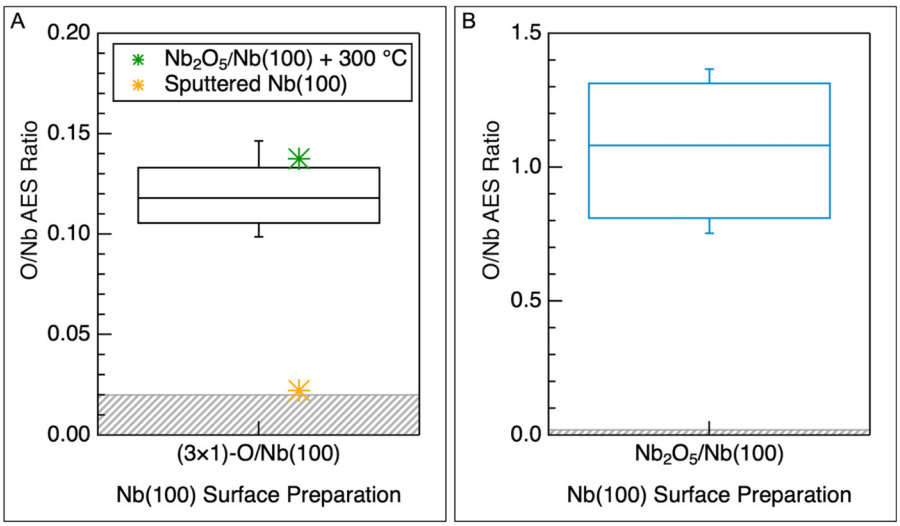

FIG. 2. O/Nb surface ratios of the (3 × 1)-O/Nb(100) and Nb_2O_5/Nb(100) surfaces from experimental AES. Box plots show calculated O/Nb ratios with the horizontal borders of each box denoting the 25th, 50th, and 75th percentiles of the (a) clean (3 × 1)-O/Nb(100) and (b) Nb_2O_5/Nb(100) surfaces. Bottom and top whiskers denote the 10th and 90th percentiles, respectively. Gray portion below O/Nb 0.02 represents the lower detection limit for AES. (a) N = 17, 50th percentile: 0.118 and (b) N = 8, 50th percentile: 1.082.

structure is a reconstruction of a NbO surface oxide and has a median Auger O/Nb ratio of 0.12 following annealing between 1600 and 1670 °C. While the (3 × 1)-O structure is highly ordered and reproducible under these annealing conditions, variations in the oxygen content arise from subsurface interstitial oxygen. The native Nb_2O_5/Nb(100) surface has a significantly larger range in surface oxygen content [Fig. 2(b)] with a median O/Nb value of 1.08. The oxygen variability of the native Nb surface arises from the amorphous nature and dependence on oxidation conditions.

To examine the Nb_2O_5 oxide dissolution process, a Nb_2O_5/Nb(100) surface was annealed at 300 °C for 1 h. The resulting O/Nb ratio is plotted as a green marker in Fig. 2(a) and closely corresponds to the NbO oxide content in the (3 × 1)-O ladder structure. This is to be expected, as Nb_2O_5 dissolution should readily occur under these annealing conditions.[12] The Nb 3d XPS region for the annealed Nb_2O_5 surface is shown in Fig. 3 along with the (3 × 1)-O/Nb(100) and Nb_2O_5/Nb(100) spectra. The Nb_2O_5 surface (blue spectra) contains the Nb $3d_{5/2}$, $3d_{3/2}$ doublets that correspond to the Nb^{+5} oxidation state at 208.0 and 210.8 eV, respectively (Table S1 in the supplementary material). The XPS spectra corresponding to the annealed Nb_2O_5 support the AES data in that the surface has fully reduced to the NbO state and is chemically synonymous with the (3 × 1)-O ladder structure.

In Fig. 4, STM images show how annealing the oxidized Nb_2O_5/Nb(100) surface for varying temperatures and durations affects the "edge" site density on the reduced NbO/Nb(100) surface. The same Nb_2O_5/Nb(100) surface that was annealed at 300 °C in Figs. 2(a) and 3 is shown in Figs. 4(a) and 4(b). We did not observe the formation of the characteristic (3 × 1)-O structure and there was very minimal long-range ordering of the NbO clusters. Figure 4(c) shows a Nb_2O_5/Nb(100) surface following an anneal at 800 °C for 1 min. The (3 × 1)-O structure formed with a high density of protruding (3 × 1)-O units that appear as bright rectangles on the terraces. Figure 4(d) shows a Nb_2O_5/Nb(100) surface following an anneal at 800 °C for 1 h in which the terrace contains a lower density of protruding (3 × 1)-O units. These protruding (3 × 1)-O units increased the density of "edge" sites across the surface, which has been shown to result in an increased nanoscale surface roughness.[19] The (3 × 1)-O edge site density for the pristine surface (T_{anneal} = 1630 °C) is shown in the first column in Fig. 4(e). The dependence of the Nb_2O_5 annealing procedure on the resulting

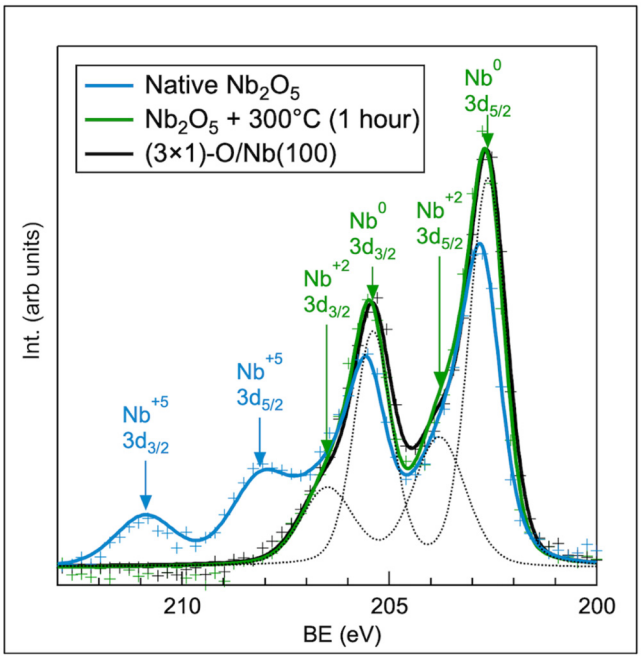

FIG. 3. Nb 3d XPS spectra of clean (3 × 1)-O/Nb(100), Nb_2O_5/Nb(100), and Nb_2O_5/Nb(100) annealed to 300 °C for 1 h. Markers represent the XPS signal, solid lines represent the fitted curves, and the dotted lines represent the individual fitted Nb^0 and Nb^{+2} 3d doublets for the clean (3 × 1)-O/Nb(100) surface.

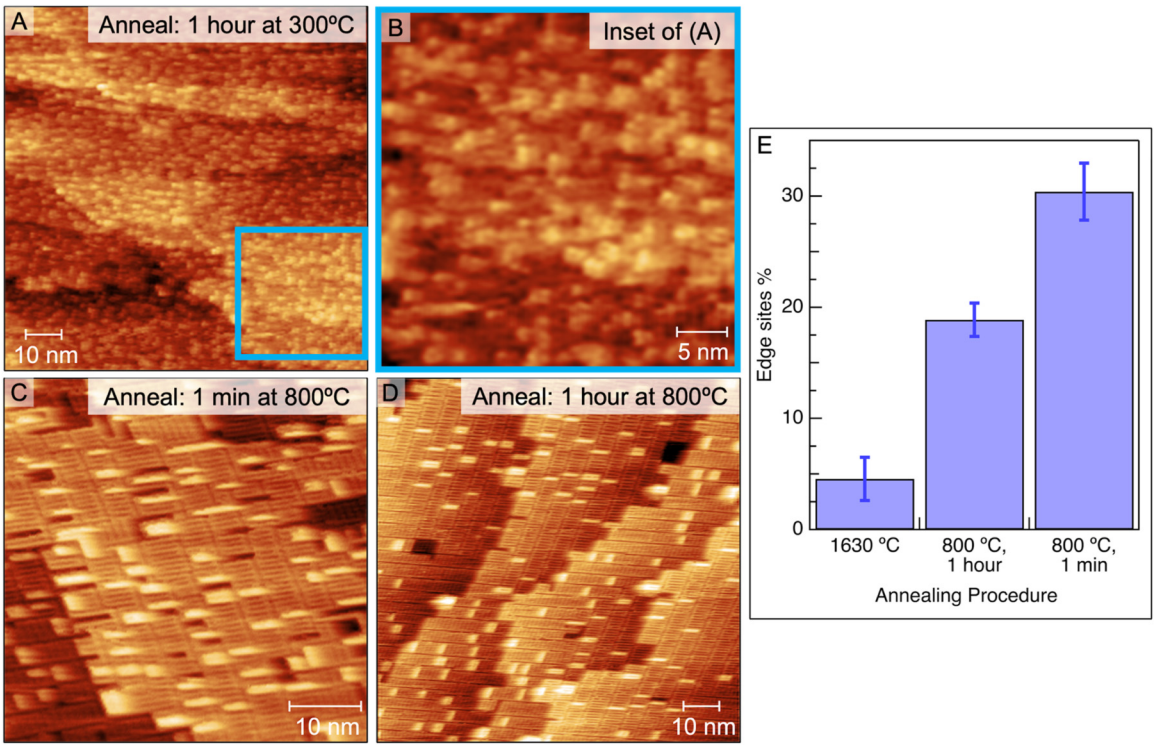

FIG. 4. STM images [(a)–(d)] and histogram (e) of the Nb_2O_5/Nb(100) surface following varying annealing procedures. Histogram in (e) shows the percentage of "edge" sites on the Nb(100) surfaces annealed to 800 °C compared to the pristine (3 × 1)-O/Nb(100) structure. (a) 300 °C for 1 h, −60.8 mV, 421 pA, 100 × 100 nm^2; (b) the inset of (a), 35 × 35 nm^2; (c) 800 °C for 1 min, −66.3 mV, 280 pA, 50 × 50 nm^2; (d) 800 °C for 1 h, 115 mV, 420 pA, 100 × 100 nm^2; and (e) histogram of the surface edge sites in (a) and (d) compared with the pristine (3 × 1)-O/Nb(100) surface.

surface defects is analogous to the tunable defect procedures from sputtering the pristine (3 × 1)-O/Nb(100) described in previously published work.[19] The temperature and duration of the Nb degas process preceding Sn exposure determines the resulting NbO binding sites that are present during the Sn nucleation step (see Table I). On the Nb(100) orientation, we observe that the "edge" sites, which preferentially nucleate Sn, form at lower temperatures and shorter annealing durations. Therefore, decreasing the temperature and duration of this degas step may result in more uniform Sn nucleation and potentially more homogeneous Nb_3Sn growth.

B. Impact of T_{dep} on ML Sn incorporation into (3 × 1)-O/Nb(100)

Figure 5 shows STM images of the (3 × 1)-O/Nb(100) surface following ML Sn exposure at elevated deposition temperatures. For 1 ML Sn deposited at T_{dep} = 780 °C [Fig. 5(a)], the Sn formed large adlayers anchored to the lower terrace at (3 × 1)-O/Nb(100) step edges. The Sn sticking coefficient [Fig. 5(a)] following 1 ML deposition at 780 °C was significantly lower than unity (~0.3), which is to be expected for this temperature regime.[20] The observed aggregation of Sn islands is very similar to sub-ML Sn coverages deposited at room temperature and annealed to 800 °C.[18] Notably, the adsorbed Sn is topographically higher, as noted in the line profile in Fig. 5(a), than the (3 × 1)-O/Nb(100) terrace, the Sn is adsorbed to. This suggests that the Sn has not incorporated into the (3 × 1)-O/Nb(100) surface and is rather adsorbed as metallic Sn. Depositing Sn at T_{dep} = 780 °C resulted in a reduced Sn coverage, with Sn desorption dominating over subsurface incorporation rates.

In Fig. 5(b), the temperature during deposition was increased 820 °C. The resulting Sn adlayer behavior is drastically different than the Sn deposited on a 40 °C lower (3 × 1)-O/Nb(100) surface in Fig. 5(a). While Fig. 5(a) shows the adsorbed Sn is simply adsorbed atop the underling (3 × 1)-O/Nb(100) terrace as evident by the line profile in Fig. 5(a), the line profile in Fig. 5(b) distinctly shows that the Sn is topographically lower than the (3 × 1)-O/Nb (100) terrace. This topographical difference between the Sn features in Figs. 5(a) and 5(b) suggests that Sn in Fig. 5(b) has incorporated into the (3 × 1)-O/Nb(100) terrace while Sn in Fig. 5(a) is simply adsorbed Sn. The Sn diffusion and incorporation into the (3 × 1)-O/Nb(100) terraces resulted in surface reconstructions, marked by narrow terraces with an increased number of step edges, due to subsurface incorporation. The higher concentration of Sn on the surface following deposition at 820 °C as compared to 780 °C confirms that Sn desorption was suppressed at this higher

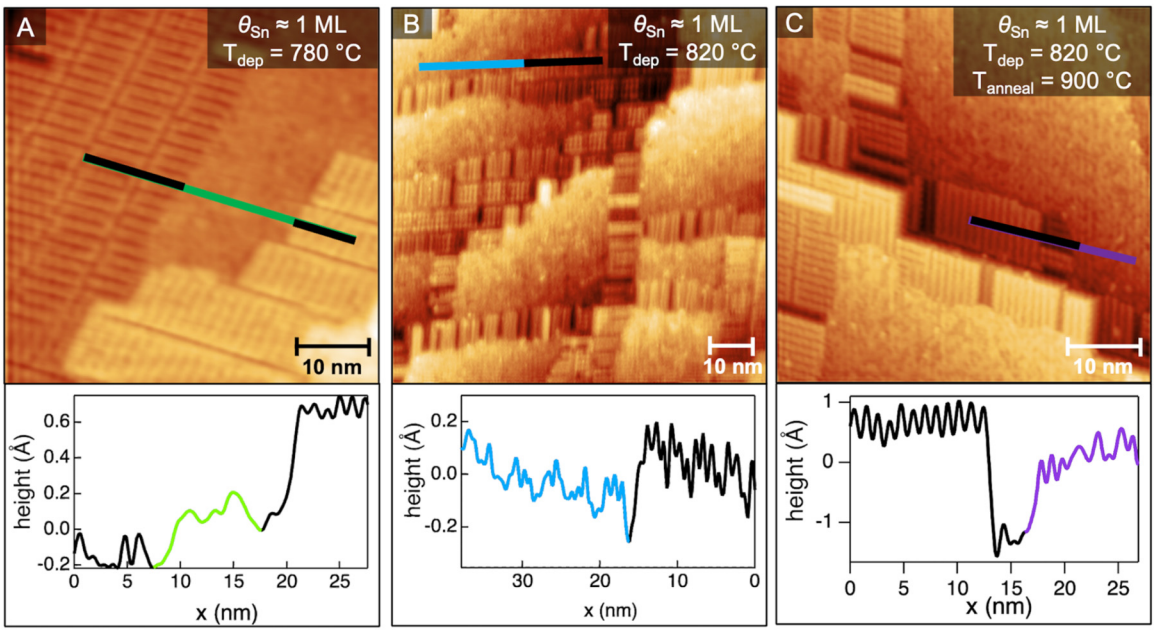

FIG. 5. STM images of the (3 × 1)-O Nb(100) surface following 1 ML Sn deposited at T_{dep} 780 and 820 °C. Inset line scans highlight the extent of subsurface incorporation by the Sn adlayer (colorful portion of line) disrupting the (3 × 1)-O/Nb(100) surface reconstruction (black portion of line). (a) T_{dep} 780 °C, 495 mV, 900 pA, 50 × 50 nm^2; (b) T_{dep} 820 °C, 128 mV, 642 pA, 80 × 80 nm^2; and (c) T_{dep} 820 °C + T_{anneal} 900 °C, 102 mV, 54.7 pA, 50 × 50 nm^2.

deposition temperature due to subsurface Sn incorporation, resulting in a Nb-Sn intermetallic phase.

In Fig. 5(c), the Sn/(3 × 1)-O/Nb(100) surface formed at T_{dep} = 820 °C was annealed for 5 min at 900 °C. This 900 °C anneal reduced the number of step edges and edge sites, thus decreasing the nanoscale roughness of the overall surface. It is also interesting to note that the Sn adlayer appeared more ordered. The Sn layer was still incorporated past the (3 × 1)-O ladder structure as evidenced by the line scan where the Sn (purple) is topographically lower than the (3 × 1)-O ladder structure (black) on the same terrace. Despite an expected decrease in the sticking coefficient for a higher deposition temperature, the promoted subsurface incorporation enhanced the thermal stability of the Sn adlayer. For ML, Sn coverages deposited at room temperature, Sn desorption occurred following a 900 °C anneal. To induce intermetallic Nb-Sn coordination at the surface, higher surface concentrations of Sn are necessary at temperatures exceeding 800 °C. The remaining Sn adlayer in Fig. 5(c) supports that an increased T_{dep} stabilizes Sn on the Nb surface at the conditions necessary for Nb_3Sn formation. For low Sn coverages probed in this study, increasing T_{dep} from 780 to 820 °C led to more favorable Sn/Nb surface interactions at this initial stage in the alloy formation process.

C. Thermal stability of 20 ML Sn deposited on Nb(100) surfaces

As was discussed in Sec. III B, the stability of Sn adlayers on oxidized Nb(100) surfaces is dependent on the surface preparation procedure, T_{dep}, and Sn coverage. In this section, 20 ML of Sn were deposited to assess the relationship between the Nb surface oxidation and Sn stability at higher Sn coverages. The Nb(100) substrate underwent three distinct Nb surface preparation procedures proceeding Sn exposure and the XPS spectra of the clean Nb surfaces are shown in Fig. 6. The formation of the native Nb_2O_5 is characterized by the Nb^{+5} doublet, as well as a Nb^{+4} contribution, indicated by the blue arrows in Fig. 6(a).[22] The O 1s peak [Fig. 6(d)] is dominated by a lower BE contribution at 530.8 eV with a secondary peak at 532 eV, indicating the presence of NbO/NbO_2 oxidation states.[23–25] The energies and widths of the fitted peaks for the Nb 3d and O 1s spectra in Fig. 6 are summarized in Tables S1 and S2 in the supplementary material.

The Nb 3d XPS region of the (3 × 1)-O/Nb(100) surface [Fig. 6(b)] contains a metallic Nb^0 and a Nb^{+2} doublet, supporting that the (3 × 1)-O/Nb(100) surface reconstruction has NbO-type character. However, the O 1s for the (3 × 1)-O/Nb(100) surface contains two distinct oxide contributions [Fig. 6(b)], suggesting that there are two distinct Nb oxide states contained in the (3 × 1)-O/Nb(100) oxide. The observation of two O 1s contributions has been previously observed for various NbO surface reconstructions and indicates that these reconstructed overlayers are electronically distinct from bulk NbO.[26–28]

To form a Nb(100) surface in the low oxygen limit, a clean (3 × 1)-O/Nb(100) surface was sputtered with Ar^+ for 5 min at 1.5 kV to remove the NbO layer. The Nb 3d XPS region following this sputtering procedure [Fig. 6(c)] suggests that the Nb surface is more reduced than the (3 × 1)-O/Nb(100) surface [Fig. 6(b)].

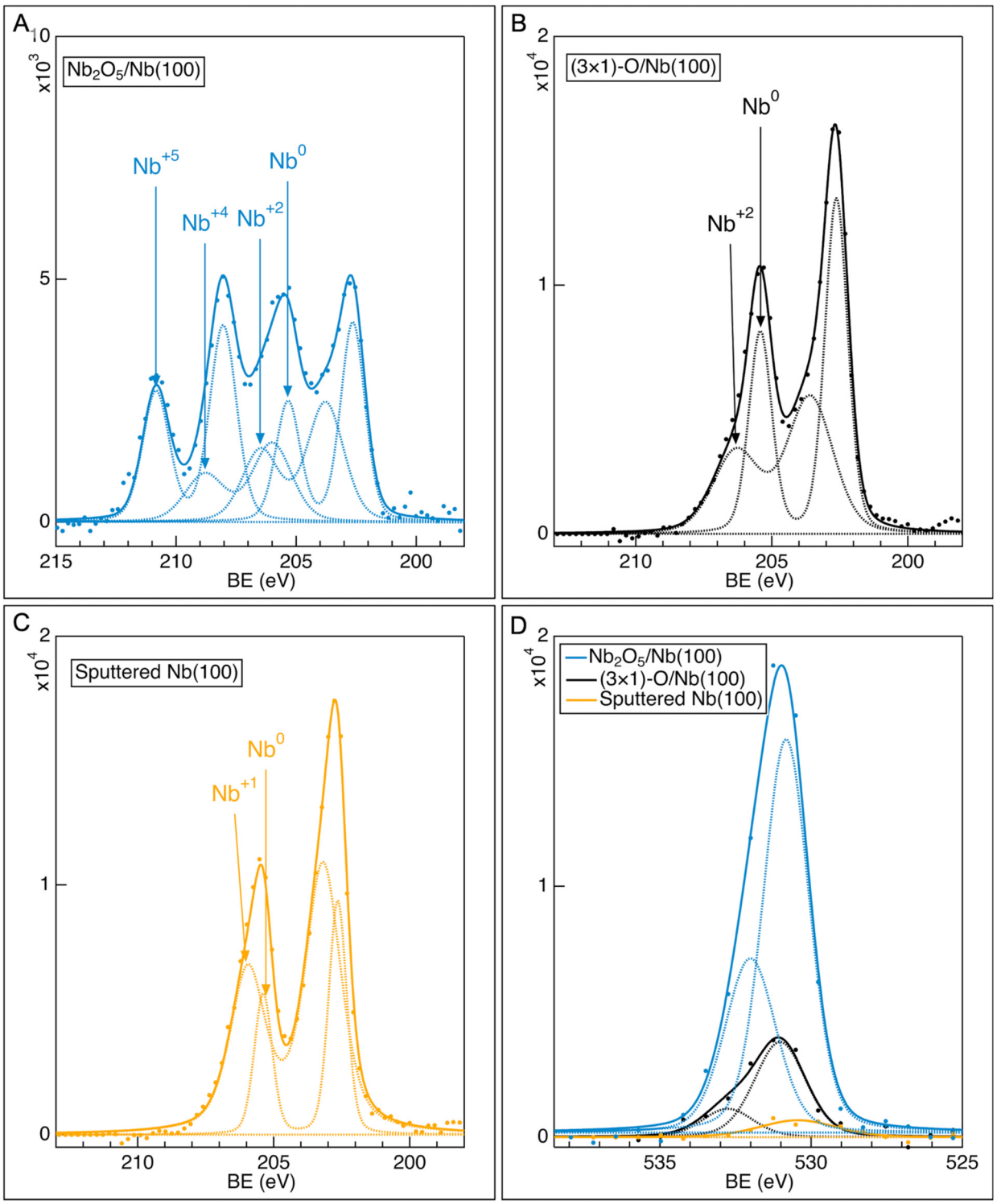

FIG. 6. XPS spectra of the varying Nb(100) surface preparations that form three distinct Nb surface oxidation states at 25 °C. Nb 3d [(a)–(c)] and O 1s (d) XPS spectra of the Nb_2O_5/Nb(100) (a), (3 × 1)-O/Nb(100) (b), and sputtered Nb(100) (c) surfaces before Sn exposure.

The higher binding energy Nb 3d doublet in the sputtered Nb(100) XPS is approximately 0.60 eV lower than the Nb^{+2} contribution on the (3×1)-O/Nb(100). Additionally, the O 1s intensity has significantly reduced following the sputtering procedure [Fig. 6(d)]. Therefore, we characterize the sputtered Nb(100) surface as a near-elemental state. This sputtered surface is not considered to be a fully metallic Nb(100) since that requires annealing at temperatures exceeding 2000 °C to promote oxygen desorption as NbO and NbO_2.[29] However, this sputtered surface does contain much less oxygen on the surface and in the near-surface region than (3×1)-O/Nb(100) as the O/Nb from AES analysis was 0.022 [Fig. 2(a)]. It is also worth noting that XPS analysis conducted immediately after sputtering did not show any appreciable carbon (Fig. S3 in the supplementary material), but it is likely that some surface contamination occurred even in UHV, as the metallic Nb is incredibly reactive.[30,31]

1. 20 ML Sn adsorption behavior on Nb(100) surfaces

In Fig. 7(a), the Sn/Nb ratios following room temperature deposition are similar for the sputtered and Nb_2O_5 surface, whereas (3×1)-O/Nb(100) has a significantly lower Sn/Nb ratio. For metal vapor deposition on a room temperature metal or metal oxide surface, we would expect near unity sticking.[32,33] This low Sn/Nb ratio observed on the (3×1)-O/Nb(100) surface is likely due to the formation of Sn islands that exposes the underlying Nb substrate and enhances the Nb contribution in the detected Auger electron signal. The higher Sn/Nb for Sn deposited at $T_{dep} = 25$ °C on the sputtered and Nb_2O_5 surfaces may result from a ML or hybrid island-ML Sn deposition mechanism. Since there does not appear to be a correlation between the amount of oxygen at the Nb surface and the resulting Sn/Nb ratio following a room temperature deposition, the Sn deposition mechanisms is likely driven by structural differences on each Nb(100) surface that determines the available Sn binding sites at surface defects. Specifically, only the "edge" sites on the pristine (3×1)-O/Nb(100) surface serve as favorable binding sites for adsorbed Sn vapor. The relatively low Sn/Nb ratio observed on (3×1)-O/Nb(100) following deposition supports that more ordered, low roughness Nb surface structures are associated with poor Sn wetting behavior. The near-elemental Nb surface was not annealed after the Ar^+ sputtering process, so the surface roughness is much higher than an annealed Nb(100) substrate.[34] The Sn/Nb Auger ratios following room temperature Sn exposure support that the nanoscale binding sites on the rougher and sputtered and Nb_2O_5 surfaces better facilitated the formation of a more uniform Sn adlayer on Nb.

The Sn 3d XPS region following deposition at $T_{dep} = 25$ °C on Nb_2O_5/Nb(100), (3×1)-O/Nb(100), and sputtered Nb(100) are plotted in Figs. 8(a)–8(c). The peak fitting conditions are summarized in Tables S3–S7 in the supplementary material. The Sn deposited on Nb_2O_5 at 25 °C partially oxidizes to SnO_2, as evidenced by the higher BE shoulder in Fig. 8(a).[35] The oxidation of the Sn is to be expected, as it is thermodynamically favorable for SnO_2 to form via partial reduction of the Nb_2O_5 layer (to NbO_2) at room temperature.[36,37] The persisting metallic Sn^0 contribution remaining after deposition is likely due to the Sn → SnO_2 reaction being kinetically limited at room temperature.[20] In Fig. 8(b), the Sn deposited on the (3×1)-O/Nb(100) surface remained in the metallic state (Sn $3d_{5/2}$: 484.9 eV).[22] At room temperature on NbO, the Sn adlayer should neither oxidize nor form an intermetallic bond with Nb.[5,20] The Sn deposited on sputtered Nb(100) at 25 °C [Fig. 8(c)] contained a minor oxide contribution to the Sn 3d spectrum.

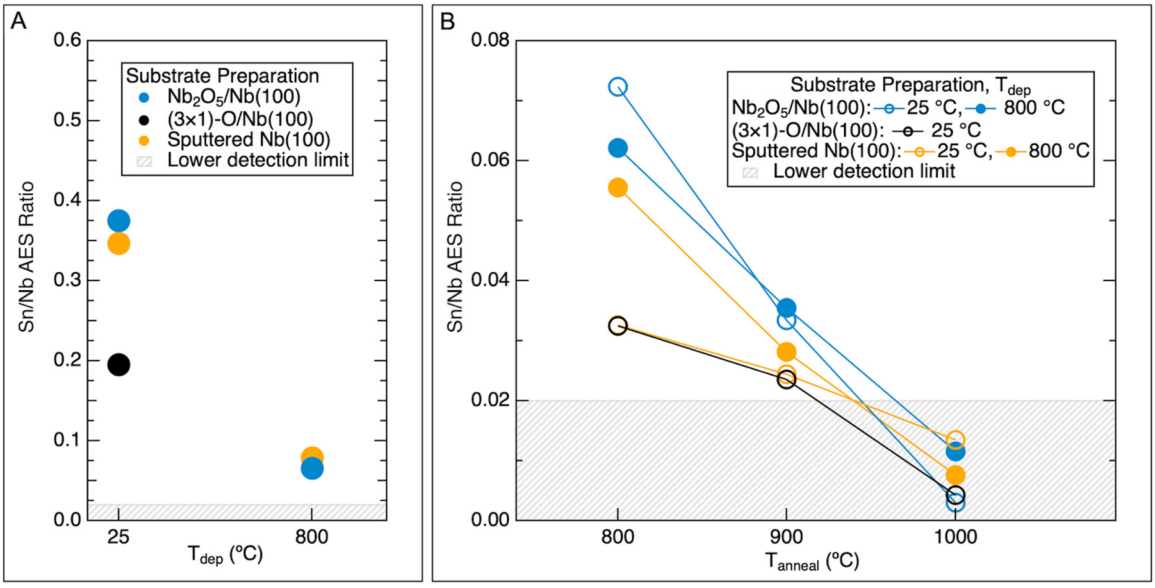

FIG. 7. Calculated Sn/Nb ratios at the Nb(100) surface immediately following Sn exposure (a) following postdeposition annealing (b) procedures. Sn/Nb ratios were calculated from experimental AES data and show that the initial Nb(100) oxidation and T_{dep} impact the Sn composition at the surface.

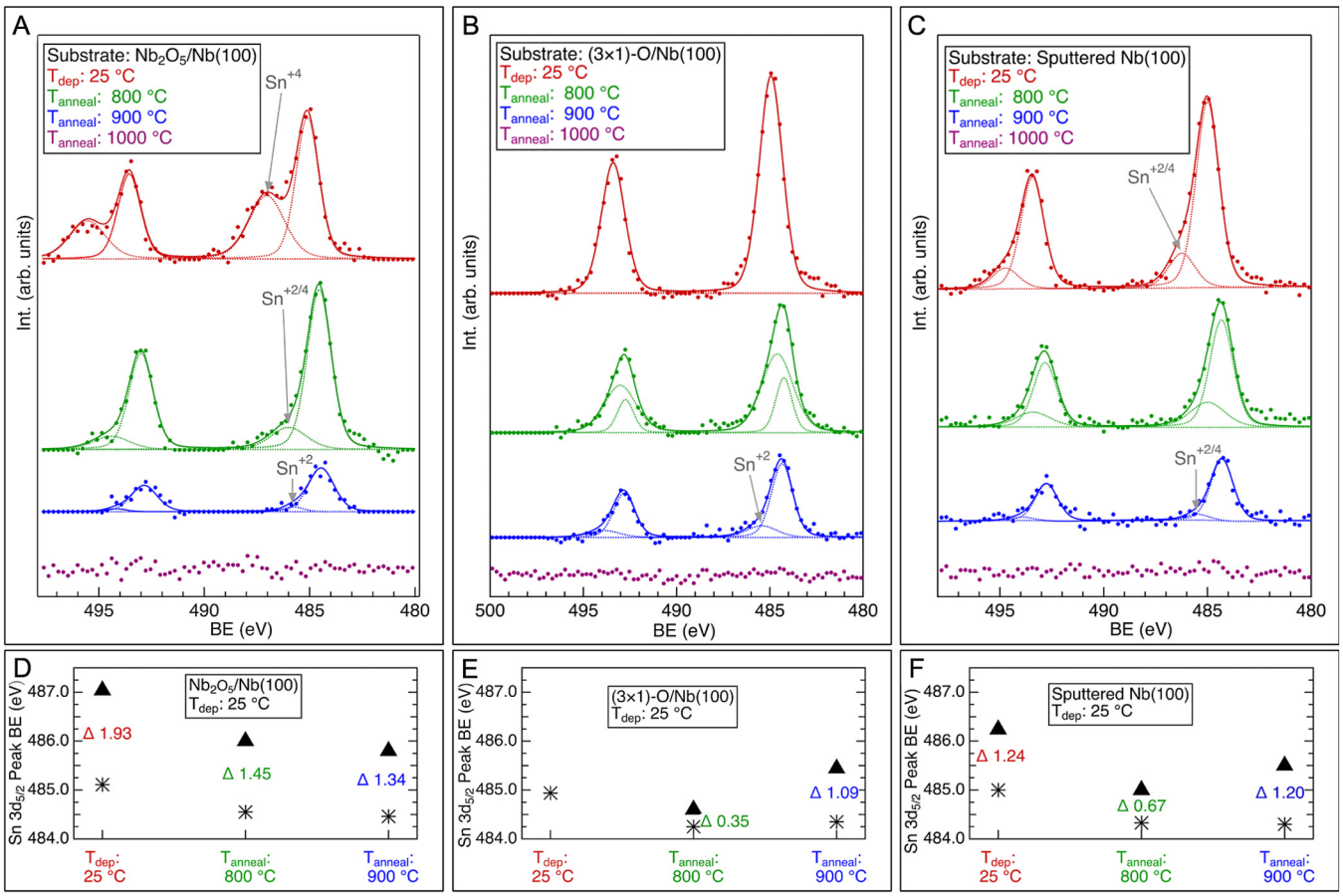

FIG. 8. Sn 3d XPS spectra [(a)–(c)] following Sn deposition (T_{dep} = 25 °C) and postdeposition annealing procedures for the indicated Nb(100) surface preparations. The initial Nb(100) surface oxidation (Fig. 6) determines the Sn adlayer oxidation following deposition at T_{dep} = 25 °C. Peak binding energies for each fitted Sn $3d_{5/2}$ contribution are shown in (d)–(f); the triangular markers correspond to the higher BE doublet and the star markers correspond to the lower BE doublet. (a) and (d) Nb_2O_5/Nb(100); (b) and (e) (3 × 1)-O/Nb(100); and (c) and (f) sputtered Nb(100).

Following Sn exposure at T_{dep} = 800 °C, we observe an expected lower Sn sticking coefficient on all Nb(100) surfaces, which is supported by the low Sn/Nb AES signals in Fig. 7(a). The Sn 3d XPS spectra following Sn deposition at T_{dep} = 800 °C [Figs. 9(a) and 9(b)] do not contain the Sn oxide contributions. However, the Sn 3d doublets have a peak binding energy (484.5–484.6 eV) that is approximately 0.4–0.5 eV lower than the expected binding energy for metallic Sn^0. Cano *et al.*[38] recently ascribed this Sn binding energy shift to the formation of a Nb-Sn intermetallic component resulting in enhanced electron density around the Sn nuclei in the A15 Nb_3Sn lattice. This reduction of the metallic Sn 3d binding energy was also observed following postdeposition anneals of the Sn/Nb(100) surfaces formed at T_{dep} = 25 °C [Figs. 8(a)–8(c)]. For the Sn/Nb_2O_5 [T_{dep} = 25 °C, Fig. 8(a)], annealing to 800 °C almost fully reduced the SnO_2 component as well. For all Sn coated Nb(100) surfaces, reaching substrate temperatures of 800 °C, either during deposition or a postdeposition anneal, resulted in a reduction of the metallic Sn 3d binding energy that is characteristic of intermetallic coordination with Nb.

2. Sn thermal stability on Nb(100) surfaces

Figure 7(b) shows the Sn/Nb AES ratios following the postdeposition annealing experiments at 800, 900, and 1000 °C. Generally, we observed a gradual decrease in the Sn surface concentration throughout the annealing process, which is likely due to Sn desorption from the Nb(100) surface. However, for the Sn deposited at T_{dep} = 800 °C on Nb_2O_5/Nb(100), the Sn/Nb ratio does not significantly changes following an anneal at 800 °C (0.065 → 0.062). There was likely still significant Sn desorption occurring in this case, but the precipitation of Sn from the subsurface may have increased the Sn Auger signal as well. After annealing to 900 °C, very little Sn persists in any of the Auger signals plotted in Fig. 7(b). The Sn/Nb ratio at 900 °C is highest for the substrates that had an initial Nb_2O_5. By

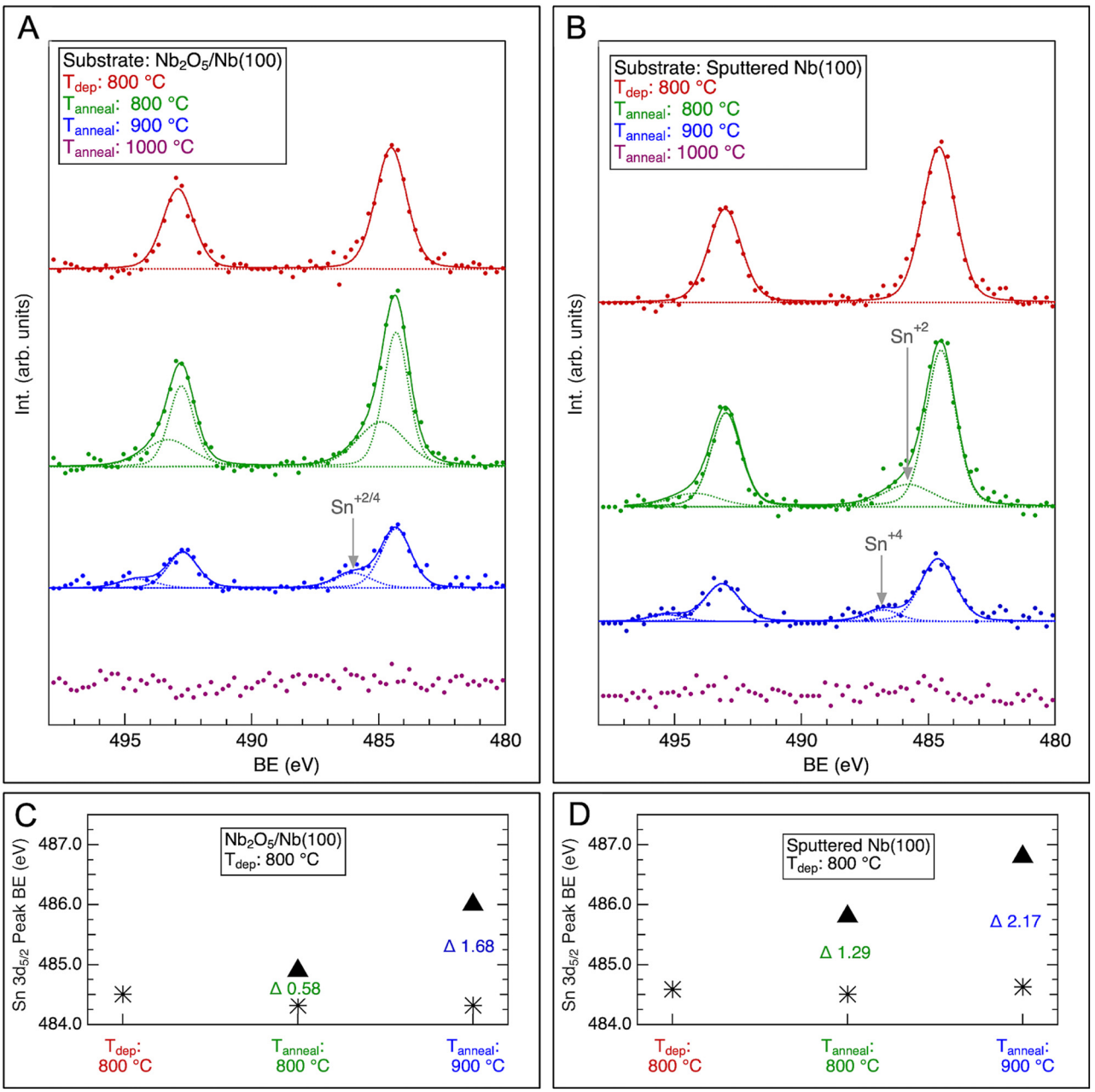

FIG. 9. Sn 3d XPS spectra [(a) and (b)] following Sn deposition (T_{dep} = 800 °C) and postdeposition annealing procedures for the indicated Nb(100) surface preparations. The initial Nb(100) surface oxidation (Fig. 6) does not significantly impact the Sn adlayer oxidation following deposition at T_{dep} = 800 °C. Peak binding energies for each fitted Sn $3d_{5/2}$ contribution are shown in (c) and (d); the triangular markers correspond to the higher BE doublet and the star marker correspond to the lower BE doublet. (a) and (c) Nb_2O_5/Nb(100) and (b) and (d) sputtered Nb(100).

1000 °C, the Sn Auger peak was comparable to the background noise and could no longer be quantified.

The XPS data confirm that the Sn fully desorbed from the Nb(100) surfaces after annealing to 1000 °C (Figs. 8 and 9). Between 800 and 900 °C, a Sn oxide shoulders appear after annealing (Figs. 8 and 9). This observation may signify that there is Sn oxide contribution to the intermetallic Nb_3Sn/Nb interface that was exposed during postdeposition annealing through Sn

desorption. An oxidized Sn species has been previously cited in the literature as a possible precursor to Nb_3Sn nucleation, pointing toward oxygen as a critical driver for Nb_3Sn growth.[39] While we observe an oxidized Sn component at the Nb interface, we are not able to assess whether the Sn oxidizes *during* the deposition process.

An alternative possibility is that the Sn oxidized during the postdeposition annealing and that the intermetallic interface was not oxidized during the deposition at $T_{dep} = 800$ °C. As described in Sec. III A, the Nb_2O_5/Nb(100) surface is fully reduced to NbO during Sn deposition at $T_{dep} = 800$ °C. However, the oxygen in the Nb_2O_5 surface dissolves into the Nb subsurface and can potentially precipitate to the formed Sn/Nb intermetallic interface upon cooling. The similar oxidation behavior of Sn deposited on the sputtered Nb(100) surface at 800 °C [Fig. 9(b)] supports that this Sn oxidization event may have occurred after deposition during the thermally induced desorption of Sn. During the Sn deposition on sputtered Nb(100) at 800 °C, at is unlikely that the hot Nb (100) contained any appreciable surface oxygen. The sputtered Nb(100) contained a very low surface oxygen concentration before Sn exposure and dissolved oxygen does not precipitate and desorb from the surface below 2000 °C.[40,41] Therefore, it is unlikely that the observed Sn oxide at the intermetallic interface formed during the Sn deposition step.

The similar adsorption and desorption pathways of Sn deposited at 800 °C on sputtered Nb(100) and Nb_2O_5/Nb(100) surfaces suggest that the initial Nb oxygen content does not promote the formation of the intermetallic interface. Rather, the higher density of favorable Sn binding sites results from the roughness of either (1) sputtering or (2) reducing Nb_2O_5 to NbO at the T_{dep}. The observed enhanced stability of Sn deposited on Nb_2O_5 at 800 °C can be attributed to the structural differences of the Nb(100) surface rather than chemical.

IV. SUMMARY AND CONCLUSIONS

In this work, we examined how the initial Nb substrate oxidation determines the NbO defect density during Sn deposition on heated Nb surfaces. We visualized with STM how increasing the deposition temperature promotes the incorporation of Sn into the Nb(100) subsurface during the temperatures necessary for alloy formation. Finally, we increased the Sn coverage to 20 ML to observe the Sn deposition and desorption behavior on varying Nb(100) surface preparations and deposition conditions with AES and XPS. Our results suggest that increasing the nanoscale defect density of the Nb surface during Sn exposure is critical for stabilizing Sn adlayers, a necessary factor in the growth of Nb_3Sn films, even at coverages exceeding 1 ML. The nanoscale defects that serve as favorable binding sites on the Nb(100) surface can be generated by lowering the annealing temperature and duration during the dissolution of the native Nb_2O_5 surface. We demonstrate that this effect is primarily structural, as we can achieve similar Sn behavior on a sputtered Nb(100) with minimal surface oxygen content. Understanding the parameters that prevent Sn loss is vital for promoting the bulk diffusion pathways that form stoichiometric Nb_3Sn during cavity coating procedures. From this work, we conclude that lowering the Nb T_{dep} during the initial introduction of Sn vapor at the nucleation stage of the standard Sn vapor diffusion recipe may result in more uniform nucleation and homogeneous Nb_3Sn film thicknesses, resulting in higher quality Nb_3Sn cavity coatings. Ongoing experimental studies aim to demonstrate the impact of altering numerous vapor and substrate conditions on the growth mechanisms and alloying dynamics that ultimately enable optimal Nb_3Sn growth. Nb_3Sn coated SRF cavities have the potential to drastically improve the efficiency and performance of existing accelerators, but this achievement is contingent upon continued elucidations of the substrate-mediated mechanisms that drive homogeneous, pristine Nb_3Sn film growth.

ACKNOWLEDGMENTS

This work was supported by the U.S. National Science Foundation under Award No. PHY-1549132, the Center for Bright Beams. NSF Materials Research Science and Engineering Center (MRSEC) at the University of Chicago, Grant No. NSF-DMR-2011854. R.G.F. thanks the University of Chicago for partial support via the Kadanoff-Rice fellowship during this work.

AUTHOR DECLARATIONS

Conflict of Interest

The authors have no conflicts to disclose.

Author Contributions

Sarah A. Willson: Conceptualization (equal); Formal analysis (lead); Investigation (equal); Methodology (lead); Visualization (lead); Writing – original draft (lead); Writing – review & editing (supporting). **Rachael G. Farber:** Conceptualization (supporting); Investigation (supporting); Methodology (equal); Writing – original draft (supporting); Writing – review & editing (supporting). **S. J. Sibener:** Conceptualization (equal); Funding acquisition (lead); Investigation (equal); Methodology (equal); Project administration (lead); Resources (equal); Supervision (lead); Writing – review & editing (equal).

DATA AVAILABILITY

The data that support the findings of this study are available from the corresponding author upon reasonable request.

REFERENCES

[1]R. Porter, T. Arias, P. Cueva, D. Hall, M. Liepe, J. Maniscalco, D. Muller, and N. Sitaraman, "Next generation Nb_3Sn SRF cavities for linear accelerators," in *Proceedings of the 29th Linear Accelerator Conference*, Geneva, Switzerland, Beijing, China, 2018 (JACOW Publishing, Geneva, Switzerland, 2019), p. 462465.
[2]J. Tiskumara, J. Delayen, G. Eremeev, U. Pudasaini, and C. Reece, "Nb_3Sn coating of twin axis cavity for SRF applications," in *Proceedings of the 20th International Conference on RF Superconductivity*, East Lansing, MI, 2021 (JACOW Publishing, Geneva, Switzerland, 2022), pp. 146–150.
[3]J. Carlson *et al.*, Phys. Rev. B **103**, 024516 (2021).
[4]R. D. Porter, D. L. Hall, M. Liepe, J. T. Maniscalco, and C. University, "Surface roughness effect on the performance of Nb_3Sn cavities," in *Proceedings of the 28th Linear Accelerator Conference (LINAC'16)*, East Lansing, MI, 2016 (JACOW Publishing, Geneva, Switzerland, 2017), pp. 32–37.
[5]A. Godeke, Supercond. Sci. Technol. **19**, R68 (2006).

[6]Y. Trenikhina, S. Posen, A. Romanenko, M. Sardela, J.-M. Zuo, D. L. Hall, and M. Liepe, Supercond. Sci. Technol. **31**, 015004 (2017).
[7]J. Lee, S. Posen, Z. Mao, Y. Trenikhina, K. He, D. L. Hall, M. Liepe, and D. N. Seidman, Supercond. Sci. Technol. **32**, 024001 (2018).
[8]U. Pudasaini, G. Eremeev, M. Kelley, C. Reece, and J. Tuggle, "Surface studies of Nb_3Sn coated samples prepared under different coating conditions," in *Proceedings of the 18th International Conference on RF Superconductivity*, Lanzhou, China, 2017 (JACOW Publishing, Geneva, Switzerland, 2018), pp. 894–899.
[9]T. Spina, B. M. Tennis, J. Lee, D. N. Seidman, and S. Posen, Supercond. Sci. Technol. **34**, 015008 (2020).
[10]U. Pudasaini, G. V. Eremeev, J. W. Angle, J. Tuggle, C. E. Reece, and M. J. Kelley, J. Vac. Sci. Technol. A **37**, 051509 (2019).
[11]D. Hall, *New Insights into the Limitations on the Efficiency and Achievable Gradients in Nb_3Sn SRF Cavities* (Cornell University, Ithaca, 2017).
[12]R. D. Veit, N. A. Kautz, R. G. Farber, and S. J. Sibener, Surf. Sci. **688**, 63 (2019).
[13]H. Oechsner, J. Giber, H. J. Füßer, and A. Darlinski, Thin Solid Films **124**, 199 (1985).
[14]B. R. King, H. C. Patel, D. A. Gulino, and B. J. Tatarchuk, Thin Solid Films **192**, 351 (1990).
[15]J. Halbritter, Electrochim. Acta **34**, 1153 (1989).
[16]J. Halbritter, "Degradation of superconducting RF cavity performances by extrinsic properties," in *Proceedings of the 11th International Conference on RF Superconductivity*, Lübeck/Travemünder, Germany, 2003 (JACOW Publishing, Geneva, Switzerland, 2003), pp. 156–162.
[17]R. E. Einziger, J. N. Mundy, and H. A. Hoff, Phys. Rev. B **17**, 440 (1978).
[18]S. A. Willson, R. G. Farber, A. C. Hire, R. G. Hennig, and S. J. Sibener, J. Phys. Chem. C **127**, 3339 (2023).
[19]R. G. Farber, S. A. Willson, and S. J. Sibener, J. Vac. Sci. Technol. A **39**, 063212 (2021).
[20]C. T. Campbell, Surf. Sci. Rep. **27**, 1 (1997).
[21]M. Ohring, *The Material Science of Thin Films* (Academic, San Diego, CA, 1992).
[22]J. F. Moulder, *Handbook of X-Ray Photoelectron Spectroscopy: A Reference Book of Standard Spectra for Identification and Interpretation of XPS Data* (Physical Electronics Division, Perkin-Elmer Corporation, Eden Prairie, MN, 1992).
[23]Z. Yang, X. Lu, W. Tan, J. Zhao, D. Yang, Y. Yang, Y. He, and K. Zhou, Appl. Surf. Sci. **439**, 1119 (2018).
[24]D. D. Sarma and C. N. R. Rao, J. Electron Spectros. Relat. Phenomena **20**, 25 (1980).
[25]S. F. Ho, S. Contarini, and J. W. Rabalais, J. Phys. Chem. **91**, 4779 (1987).
[26]A. S. Razinkin, E. V. Shalaeva, and M. V. Kuznetsov, Phys. Met. Metallogr. **106**, 56 (2008).
[27]S. Berman, A. Zhussupbekova, B. Walls, K. Walshe, S. I. Bozhko, A. Ionov, D. D. O'Regan, I. V. Shvets, and K. Zhussupbekov, Phys. Rev. B **107**, 165425 (2023).
[28]K. Zhussupbekov *et al.*, Sci. Rep. **10**, 3794 (2020).
[29]B. An, S. Fukuyama, K. Yokogawa, and M. Yoshimura, Phys. Rev. B **68**, 115423 (2003).
[30]R. G. Musket, W. McLean, C. A. Colmenares, D. M. Makowiecki, and W. J. Siekhaus, Appl. Surf. Sci. **10**, 143 (1982).
[31]T. W. Haas, Surf. Sci. **5**, 345 (1966).
[32]M. Bäumer and H.-J. Freund, Prog. Surf. Sci. **61**, 127 (1999).
[33]D. G. Van Campen and J. Hrbek, J. Phys. Chem. **99**, 16389 (1995).
[34]D. Marton and J. Fine, Thin Solid Films **185**, 79 (1990).
[35]M. A. Stranick and A. Moskwa, Surf. Sci. Spectra **2**, 50 (1993).
[36]K. T. Jacob, C. Shekhar, M. Vinay, and Y. Waseda, J. Chem. Eng. Data **55**, 4854 (2010).
[37]E. G. Lavut, B. I. Timofeyev, V. M. Yuldasheva, E. A. Lavut, and G. L. Galchenko, J. Chem. Thermodyn. **13**, 635 (1981).
[38]A. Cano, G. V. Eremeev, J. R. Zuazo, J. Lee, B. Luo, M. Martinello, A. Romanenko, and S. Posen, J. Phys. Chem. C **127**, 19705 (2023).
[39]Z. Sun, D. K. Dare, Z. Baraissov, D. A. Muller, M. O. Thompson, and M. U. Liepe, APL Mater. **11**, 071118 (2023).
[40]G. Ciovati, Appl. Phys. Lett. **89**, 022507 (2006).
[41]E. M. Lechner, J. W. Angle, A. D. Palczewski, F. A. Stevie, M. J. Kelley, and C. E. Reece, J. Appl. Phys. **135**, 133902 (2024).